Ultrahigh-Performance Osmotic Power Generation in Gate-Controlled Nanopores

Lei, Xin; Zhang, Jiayan; Hong, Hao; Liu, Zewen; Huang, Yu; Xia, Fan; Mao, Liang; Jiang, Lei

DOI
10.1002/adfm.202500989

Publication date
2025

Document Version
Final published version

Published in
Advanced Functional Materials

ADVANCED FUNCTIONAL MATERIALS
www.afm-journal.de

Ultrahigh-Performance Osmotic Power Generation in Gate-Controlled Nanopores

Xin Lei, Jiayan Zhang, Hao Hong, Zewen Liu, Yu Huang, Fan Xia, Liang Mao, and Lei Jiang*

The osmotic energy, as a representative of sustainable clean energy, has provided promising strategies to the energy shortage and the environmental pollution. Via selectively diffusing (cations or anions) through the porous membrane, the osmotic energy can be converted into electricity directly. Nevertheless, the energy-conversion efficiency is significantly limited in the lower surface charge at the membrane surface. In response, here a novel gate-controlled nanopore (field effect transistor-like) as an efficient osmotic generator is exploited. With real-time application of negative gate voltages, the surface charge density is accurately enhanced by an order of magnitude from −0.01 to −0.1 C m^{-2} while maintaining an effective salinity difference. Based on that, the single-pore osmotic power is amazingly boosted by four orders of magnitude, reaching the summit of 2.90 nW, which outperforms the state-of-the-art 2D system represented by single-layer MoS_2 of 1 nW. Further expanding into porous membranes, the corresponding power density reaches the pioneering of 1008 W m^{-2}, far more exceeding the commercial standard of 5 W m^{-2}. Obviously, this work gives an underlying insight into ionic transport in confined nanochannels, as well as providing an alternative template for efficient osmotic energy generation.

1. Introduction

Climate change, driven by the excessive emission of greenhouse gases, poses an alarming threat to human survival, exacerbated by ongoing urban modernization and global industrialization.[1] To address this vital crisis, the complete transition from fossil fuels to clean energy is crucial for the effective reduction of greenhouse gas emissions at their source.[2] However, the reliability of certain clean energy, such as solar and wind,[3] is overly dependent on unpredictable weather conditions, which places additional demands on the stability of the energy supply. In response, "osmotic energy" has emerged as a stable platform for electricity generation, utilizing natural salinity gradients, supported by its consistent production, significant reserves, and widespread availability.[4] According to statistics, the global reserve of osmotic energy generated by the mixing of river and seawater reaches up to 1.0 TW, surpassing the combined output of solar and wind energy.[5] Remarkably, up to 0.8 kW m^{-3} of osmotic power can be extracted, which is comparable to the energy produced by water falling from dams over 280 m high.[6] Harvesting osmotic energy is dependent on effective energy-conversion technologies, and the reverse electrodialysis (RED)[7] system has attracted widespread interest due to its direct conversion without intermediate processes.

In this system, the primary task for efficient power generation is to develop porous membranes that exhibit both higher

X. Lei, J. Zhang, L. Jiang
Key Laboratory of Bio-Inspired Smart Interfacial Science and Technology of Ministry of Education
School of Chemistry
Beihang University
Beijing 100191, P. R. China

H. Hong
Department of Microelectronics
Delft University of Technology
Delft 2628 CD, The Netherlands

H. Hong, Z. Liu
School of Integrated Circuits
Tsinghua University
Beijing 100084, P. R. China

Y. Huang, F. Xia
State Key Laboratory of Geomicrobiology and Environmental Changes
Engineering Research Center of Nano-Geomaterials of Ministry of Education, Faculty of Material Science and Chemistry
China University of Geosciences
Wuhan 430074, P. R. China
E-mail: yuhuang@cug.edu.cn

L. Mao
State Key Laboratory of Pollution Control and Resource Reuse
School of the Environment
Nanjing University
Nanjing 210023, P. R. China

L. Jiang
CAS Key Laboratory of Bio-inspired Materials and Interfacial Science
Technical Institute of Physics and Chemistry
Chinese Academy of Sciences
Beijing 100190, P. R. China

The ORCID identification number(s) for the author(s) of this article can be found under https://doi.org/10.1002/adfm.202500989

DOI: 10.1002/adfm.202500989

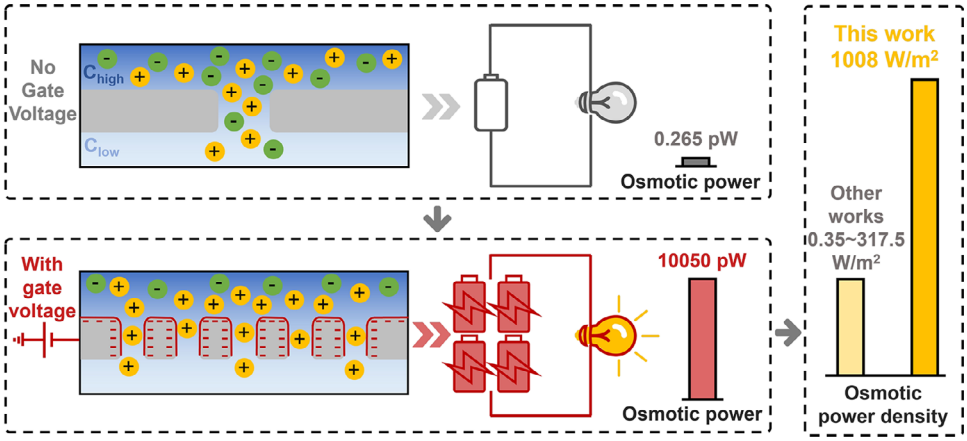

Scheme 1. The gate-controlled nanopore is an efficient osmotic energy generator. The application of gate voltage increased the surface charge density of the nanopore by an order of magnitude, leading to highly selective ion diffusion from C_{high} to C_{low}. This process enabled the efficient conversion of osmotic energy into electrical energy, with osmotic power rising from 0.265 to 10050 pW. Additionally, the osmotic power density reached an impressive 1008 W m^{-2}, exceeding the performance of previous works.

ion selectivity indicated by the osmotic voltage and higher ion permeability indicated by the osmotic current. Initially, a power density of only 0.17 mW m^{-2} was achieved using a conventional assembly of exchange membranes (IEMs) for both anions and cations.[8] To improve the performance, researchers have further adjusted the surface composition and optimized the membrane structure. Nijmeijer et al.[9] enhanced ion selectivity by introducing tertiary diamines into the ion exchange groups at the membrane surface, resulting in an increase of power density to 1.27 W m^{-2}. In the improvement of ion permeability, Wen et al.[10] developed polyether sulfone/sulfonated polyether sulfone membranes containing a large number of nanochannels, achieving a power density of 2.48 W m^{-2}. With the advancement of commercialization, more mature materials were developed for osmotic energy generation, including Nafion membranes (Quintech),[11] AEM, and CEM membranes (Fujifilm),[12] due to their sufficient mechanical strength and low cost. However, the micron-scale thickness of these membranes and disordered discontinuous pore structures severely affected the ion permeability, which in turn limited the power density below the commercial standard (5 W m^{-2})[6] for practical applications.

The emergence of solid-state nanopores has created opportunities to overcome the aforementioned limitations, by utilizing the Micro-electromechanical System (MEMS) process. This technique allowed for the reliable preparation of Si_3N_4 and SiO_2 membranes with thicknesses down to 10 nm.[13] These membranes were even capable of supporting single-layer 2D materials with sub-nanometer thicknesses, such as graphene,[14] boron nitride (BN),[15] and molybdenum disulfide (MoS_2)[16] for higher ion permeability. Subsequently, porous membranes with well-ordered and aligned nanostructures could be accurately fabricated, through focused ion beam (FIB) etching with single-nanometer resolution and direct visual feedback.[17] However, there has been limited research utilizing this technology to achieve consistently efficient osmotic energy generation from a single pore to porous membranes, by regulating the magnitude and distribution of surface charge density in real-time (improving ion selectivity) while maintaining the maximized porous density (improving ion permeability). Meanwhile, a gate-controlled nanopore with field effect has been widely developed.[18] By adjusting the gate voltage, the surface potential at the nanopore/liquid interface could be effectively controlled, leading to ion redistribution, which in turn affected ion conductivity, fluid flow, and particle transport.[19] Based on that, gate-controlled nanopores were widely used in ion-selective transport,[20] ion rectification,[21] microfluidics,[22] and particle sensing.[23] Particularly in sensing, gate-controlled nanopores provided a high-sensitivity and integrable method for label-free detection of biological species in solutions or complex biological media.[24] With the widespread participation of 2D materials, the ultra-thin thickness (only 0.335 nm in graphene) and high electron mobility made DNA sequencing possible.[25]

Inspired by this, we developed a novel gate-controlled nanopore (field effect transistor-like) as an efficient osmotic generator in **Scheme 1**, using MEMS processes combined with single-nanoscale FIB sculpting. Taking advantage of the real-time control of gate voltage, the surface charge density was effectively enhanced while maintaining an effective salinity difference, boosting the single-pore power by four orders of magnitude to an outstanding performance of 2903 pW. Meanwhile, controlling the charging regions both on the inner pore wall and outer membrane surface surrounding the nanopore, assisted with the optimized single-pore size, resulted in a congenerous enhancement of ion selectivity and ion permeability. Further promoting from the single pore to porous membranes, the corresponding power density reached the pioneering of 1008 W m^{-2} on the global scale, via balancing the nanoporous density (affecting ion permeability) and the inter-pore effect (affecting ion selectivity). Last but not least, this paper gained an insight into the key roles that significantly influence the generation performance of membranes from experiments to simulations, while providing valuable guidance on efficient osmotic energy generation. Notably, the gate-controlled nanopores not only presented excellent energy-conversion performance and mechanical properties but also offered available templates for traditionally low-efficiency materials.

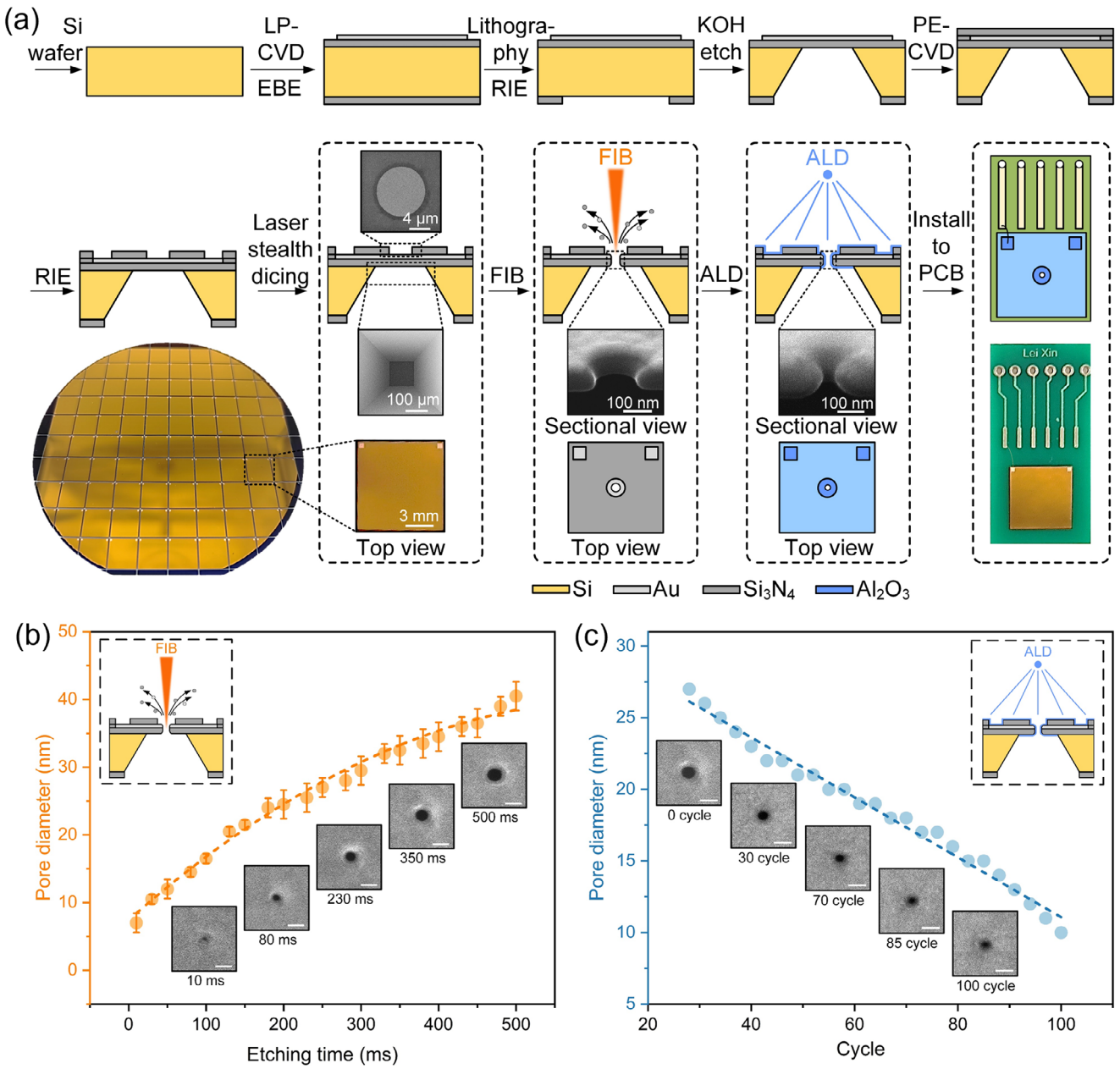

Figure 1. The preparation of the gate-controlled nanopore based on multi-step MEMS processes. a) Via layer-by-layer deposition and multi-step etching of different materials, suspended nanofilms were built up; Then nanopores were generated on that film using FIB etching and ALD deposition; finally, they were encapsulated on PCB linking the external circuit to constitute a transistor-like nanopore (Si_3N_4 was insulating layer; Au was gate-electrode layer; Al_2O_3 was gate-dielectric layer). b) By increasing the etch time of FIB (beam current of 5 pA, accelerating voltage of 30 kV), the nanopore size gradually rose from a minimum of 7 nm to more than 40 nm, while the growing rate gradually slowed down. The scale bar was 50 nm. c) The nanopore size was linearly reduced from 31 nm to less than 10 nm by adding the deposition cycle of ALD (reaction temperature of 200 °C). The scale bar was 50 nm.

2. Results and Discussion

2.1. Controllable Fabrication of Gate-Controlled Nanopores

Figure 1 clearly illustrates the preparation of the gate-controlled nanopore based on multi-step MEMS processes. A 50 nm-thick Si_3N_4 and a 30 nm-thick layer of Au, serving as insulating and gate electrodes respectively, were sequentially deposited on 4-inch silicon wafers by low-pressure chemical vapor deposition (LP-CVD) and electron beam evaporation (EBE). Subsequently, the backside Si was exposed by photolithography and reactive ion etching (RIE), followed by KOH anisotropic etching along the (111) plane until the suspended Si_3N_4/Au nanofilms (100 μm × 100 μm) were formed. Returning to the front, the insulation Si_3N_4 was further improved by plasma-enhanced chemical vapor deposition (PE-CVD). Additionally, RIE was employed to

expose the Au layer at the center (10 µm diameter) for nanopore fabrication. Meanwhile, the Au layer at the edge was patterned for gate voltage connections to the external circuit. Finally, the entire wafer was divided into ≈70 nanofilms (9 mm × 9 mm) using laser stealth dicing, as shown in Figure 1a. It was noteworthy that the critical nanopores were precisely located and fabricated at the center of the nanofilm using a focused ion beam (FIB) with single-nanometer precision. Combined with self-limiting atomic layer deposition (ALD) at sub-nanometer precision, a 20 nm-thick gate dielectric Al_2O_3 was deposited to completely encapsulate the exposed Au layer, forming a mimic gate-around field effect transistor (FET), as illustrated in the cross-sectional view of Figure 1a. Then, the nanofilm was mounted on the PCB and connected with the external circuit through wiring, directly providing the gate voltage. This setup allowed for easy modulation of the surface charge density of the nanopores. The detailed processing steps and parameters are further shown in Figure S1 (Supporting Information). In this process, precise control of the nanopore size played a crucial role in subsequent osmotic energy generation. Benefiting from single-nanoscale etching precision (less than 3 nm, Ga^+) and extremely higher imaging resolution (0.5 nm, He^+), FIB facilitated accurate modulation of nanopore size and 3D morphology in multilayer through programmable ion dose distribution.[17] By increasing the etch time in increments of 10 ms, the initial size of the nanopore increased from a minimum of just 7 nm to over 40 nm, as shown in Figure 1b. Moreover, the highly efficient fabrication (only 10 ms for the single pore) with programmable etching positions facilitated high-throughput preparation and practical application of nanopore arrays. Subsequently, the nanopore size was further reduced with sub-nanometer precision through the ALD deposition of gate-dielectric Al_2O_3. A linear reduction in nanopore size was observed, from the initial 32 nm to less than 10 nm, by gradually increasing the number of deposition cycles to 100, as shown in Figure 1c. Taking advantage of the self-limiting growth of ALD, the deposition rate was maintained at 0.11 nm per cycle, enhancing dimensional control accuracy. In summary, the gated-controlled nanopore with a minimum diameter of 10 nm was successfully prepared based on multi-step MEMS processes.

2.2. Osmotic Energy Generation Based on Gate-Controlled Nanopores

Figure 2a comprehensively illustrates the osmotic energy generation platform based on the gate-controlled nanopore. KCl solution with concentration difference was placed on both sides of the nanopore (C_{high} in *Cis* and C_{low} in *Trans*). The nanopore was served as the sole channel for ion diffusion, thus generating the ionic current. The *Cis* and *Trans* compartments were equipped with Ag/AgCl electrodes as the source and drain, respectively, forming a circuit for ion current (I_{ion}) measurement under bias voltage (V_b) at the source. Meanwhile, the Au layer in the nanopore was directly connected to the gate voltage in an external circuit, which was designed to regulate the surface charge density of the nanopore for efficient osmotic energy generation. In this setup, the short-circuit current (I_{sc}) and open-circuit voltage (V_{oc}) were obtained by measuring the I_{ion}-V_b response resulting from the selective diffusion of ions. After subtracting the contributions from the electrode/solution interface at different concentrations (calculated by the Nernst equation,[26] See Figure S2 and Table S1, Supporting Information for details), the pure osmotic potential (V_{os}) and osmotic current (I_{os}) were determined. Additionally, the osmotic power (P_{os}) was strictly calculated by subtracting the proportion of the input power, as shown in Figure S3 (Supporting Information).

In detail, without the gate voltage, there was only a slight positive current (I_{sc} = 10 nA) due to the weakly negative charged nanopore surface (−0.01 C m^{-2}), as shown in Figure 2b. Upon applying a gate voltage of −300 mV, the surface charge density of the nanopore surface increased by an order of magnitude (−0.1 C m^{-2}), as later confirmed, resulting in significant enhancement of K^+ selectivity, with K^+ diffusion dominating in the nanopores. Both the V_{os} (from 2.5 to 83 mV) and the I_{os} (from 0.122 to 42 nA), particularly the osmotic power (P_{os}), which increased by four orders of magnitude from 0.265 to 2903 pW, showed significant improvements, as shown in Figure 2c. This enhancement was not only due to the higher surface charge density induced by the gate voltage but also to the presence of a specific charging region on the inner pore wall, particularly on the outer membrane surface surrounding the nanopore. This region was crucial for maintaining high ion selectivity and a concentration difference, as proved in Figure S4 (Supporting Information) and supported by the Poisson-Nernst-Planck (PNP) model[27] detailed in Methods S1 (Supporting Information). We also evaluated the charging range necessary for different surface charge densities (e.g., −0.1 C m^{-2} corresponds to 1578 nm in Figure S6, Supporting Information). This evaluation was crucial for optimizing the density of nanopore arrays in practical applications to minimize mutual interference and achieve the highest power density. By effectively controlling the porous array gap (with a porosity of 5.7%) and maintaining a gate voltage of −300 mV, the osmotic power P_{os} was further increased from 497 to 10050 pW, representing the maximum power density, as shown in Figure 2d. This enhancement was primarily due to the parallel arrangement of nanopores, which increased ion flux and resulted in a rise in I_{os} from 42 to 228 nA. Additionally, the current direction (ion selection polarity) could be easily reversed in the gate-controlled nanopore. As shown in Figure 2e, reversing the polarity of the gate voltage simultaneously shifted the cation selectivity to anion selectivity. The reversal also led to an immediate change in the direction of the IV response, with both I_{sc} and V_{oc} being inverted, resulting in a generation power of 497 pW. In summary, the gate-controlled nanopore platform provided a more convenient and real-time tuning mechanism, enabling highly efficient osmotic energy generation. Compared with conventional approaches, it simplified the process by eliminating the need for repeated modifications and de-modifications.

2.3. Ion-Transport Characteristics of Gate-Controlled Nanopores

To gain a deeper understanding of the gate-controlled nanopore, ion-transport characteristics of nanopores were further investigated under varying ionic concentrations and gate voltages. **Figure 3a** presents the I_{ion}-V_b response of nanopores without gate voltage. As the ion concentration increased from 10^{-6} to 1 M (with conductivity rising from 3.41 × 10^{-5} to 1.10 S m^{-1}), the linear

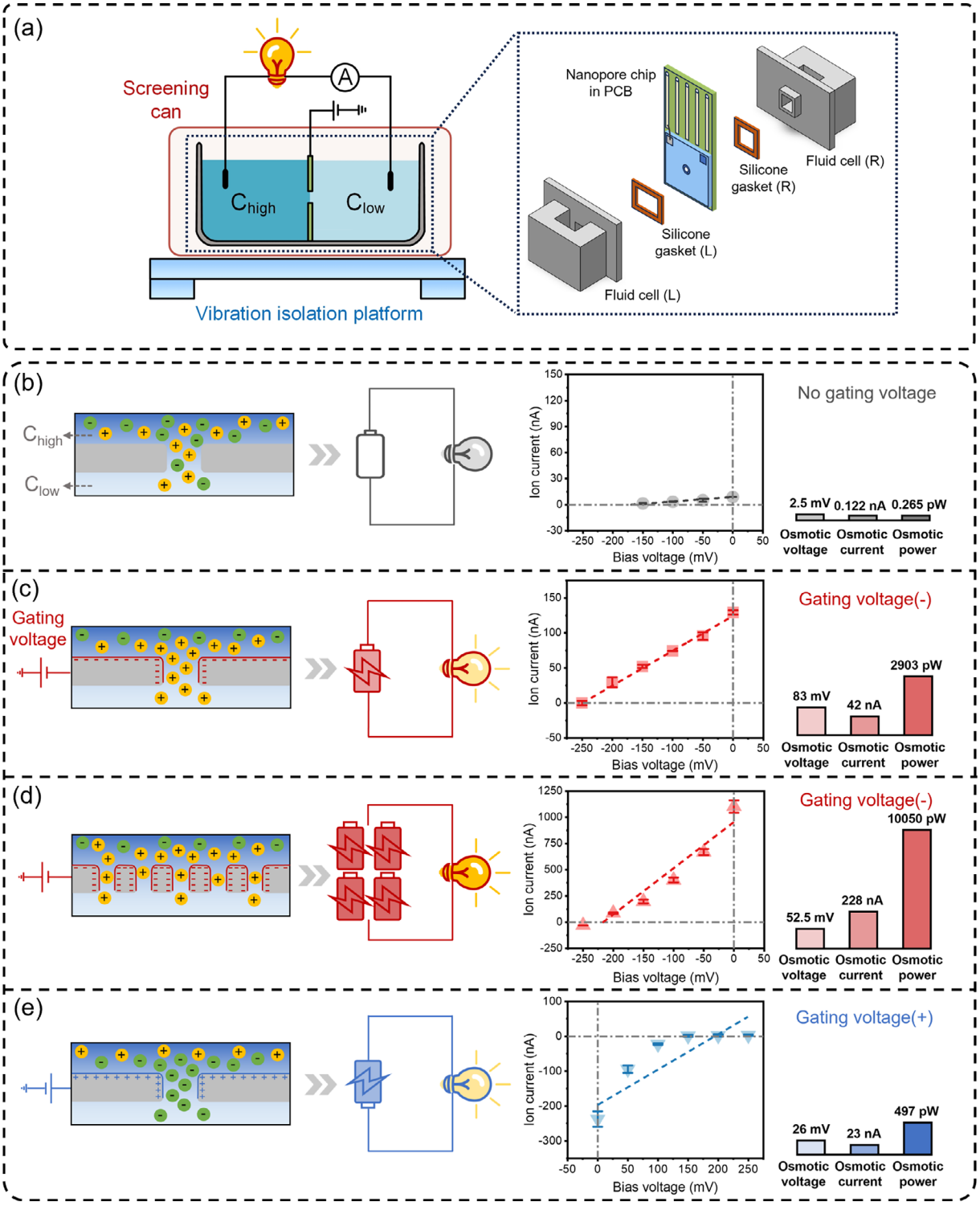

Figure 2. a) The osmotic energy generation platform based on the gate-controlled nanopore. Via the application of gate voltage, the surface charge density of the nanopore was first enhanced. Then through highly ionic-selective diffusion from C_{high} to C_{low}, efficient conversion from osmotic energy to electrical energy was achieved. b) Without the gate voltage, almost non-selectively synchronous diffusion of positive and negative ions produced limited osmotic energy generation (0.265 pW). c) After applying the negative gate voltage, higher osmotic energy generation (2903 pW) was yielded owing to more diffusion of the positive ions relative to the negative. d) Further increasing the nanopore density resulted in greater osmotic energy generation (10050 pW). e) Following an inverted polarity of the gate voltage, the corresponding ion selectivity was flipped instantly, resulting in a reversal of direction of the I_{ion}-V_b response. In summary, taking advantage of the real-time control of gate voltage, the surface charge density was effectively enhanced, boosting the generation power to outstanding performances.

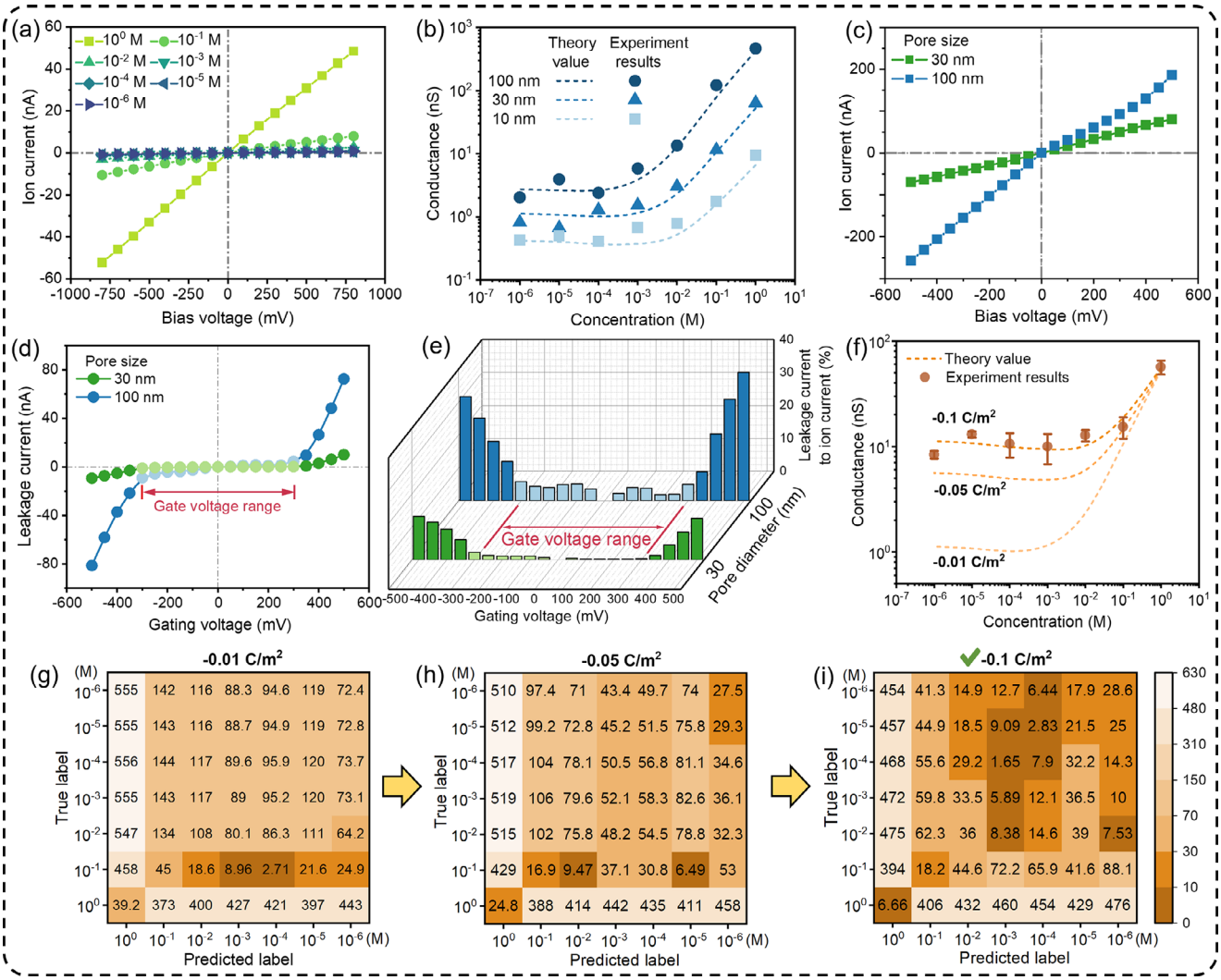

Figure 3. Ion-transport characteristics of the gate-controlled nanopore. a) Without gate voltage, the slope of the I_{ion}-V_b response ramped up with stronger ion concentration. b) The experiment results of nanopore conductivity were consistent with theory values (dominated by bulk conductance at higher concentrations whereas surface conductance at lower concentrations). c) The ion currents between the source and drain were tested by applying only the bias voltage at the source instead of the gate. The salt concentration was 1 M. d) Under the application of gate voltage, a sudden change of leakage current was detected between the gate and the drain. Ultimately, the gate range was determined from −300 to +300 mV. The salt concentration was 1 M. e) The accuracy of this gate range was further verified by the ratio of the leakage current to the ion current. f) Since the imposing of gate voltage, experiment results of nanopore conductance kept pace with fresh theory values at the surface charge density of −0.1 C m^{-2} rather than the previous −0.01 C m^{-2}. g–i) Furthermore, the confusion matrix certificated confirmedly that the surface charge density did enhance to −0.1 C m^{-2} under the gate voltage (vertical axis was the experiment result; horizontal axis was the theory value at different surface charge density; the darker the color, the more similar the corresponding values were; the dark color closer to the main diagonal meant that the experiment results matched the predicted values more precisely). In summary, the application of gate voltage resulted in an effective enhancement of the surface charge density from −0.01 to −0.1 C m^{-2}, as verified by both experimental and theoretical equations.

relationship between I_{ion} and V_b becomes more pronounced, indicated by a gradually steeper slope. Furthermore, we experimentally determined the ionic conductivities of nanopores with varying diameters of 10, 30, and 100 nm at different concentrations, and compared these with theoretical values:[28]

$$G = \kappa_b \left[\frac{4L}{\pi D^2} \times \frac{1}{1 + 4\frac{l_{D_u}}{D}} + \frac{2}{\alpha D + \beta l_{D_u}} \right]^{-1} \quad (1)$$

Here, κ_b denoted the bulk conductivity, while L and D represented the length and diameter of the nanopore, respectively. To highlight the significance of surface conduction compared relative to bulk conduction, Dukhin length $l_{D_u} \approx (|\Sigma|/e)/(2c_s)$ was introduced, where Σ denoted the surface charge density and c_s was the salt concentration. The geometrical factor $\alpha = 2$ was consistent with values reported in the literature.[28] While the adjustable parameter β was ≈4 with the best fit to the experimental results. There is room for adjustment and variable-free parameters. It is acceptable to make small adjustments to the free

parameter β based on actual experimental results as a reference. As shown in the matching results in Figure 3b, the experimental pore conductance values were highly consistent with the theoretical predictions for a surface charge density of −0.01 C m^{-2}, in the absence of gate voltage. This was in agreement with the previously reported surface charge density of natural Al_2O_3, which is ≈−10 mC m^{-2} at pH = 7.6.[29] Additionally, the saturation platform of nanopore conductance indicated the presence of a charged nanopore surface, characterized by an electrical double layer (EDL).[30] At higher concentrations, nanopore conductance was dominated by bulk conductance, which varied linearly with ionic concentration. At lower concentrations, surface conductance gradually became dominant as the EDL thickness became comparable to the pore size, leading to a saturated platform. For small nanopores (10 nm diameter, 5 nm radius), the ion concentration gradually saturated starting from 10^{-2} M, corresponding to an EDL thickness of 3.1 nm.[30] In contrast, for larger nanopores (100 nm diameter, 50 nm radius), the ion concentration must be lower than 10^{-4} M to achieve a thicker layer EDL, with a thickness of 30.5 nm.[30]

Moreover, to thoroughly investigate the gate-controlled modulation of surface charge density, it is necessary to determine the appropriate range of the gate voltage in advance. Initially, linear ion currents between the source and drain were measured by applying a bias voltage solely at the source, shown in Figure 3c. Subsequently, the leakage current between the gate and drain was monitored by varying the gate voltage while keeping the source unbiased. As shown in Figure 3d, the leakage current remained extremely low across a range of gate voltages from −300 to +300 mV. However, the leakage current increased rapidly once the threshold voltage (±300 mV) was exceeded, contrasting sharply with the linear ion current observed under bias voltage. Figure 3e illustrates the proportion of the leakage current to the ionic current at the same voltage, which remained below 10% of the ionic current up to the threshold (300 mV) and then increased progressively beyond it. This transistor-like behavior characteristic, where current amplification occurred only beyond a certain threshold voltage, had also been reported in other nanopore research.[18] Consequently, the gate voltage was constrained between −300 and +300 mV to prevent dielectric breakdown and excessive intervention of leakage current.

Furthermore, by applying the maximum gate voltage of −300 mV, the variation of ionic conductance in nanopores was investigated, as shown in Figure 3f. It was observed that the nanopore conductance at lower concentrations deviated significantly from the original theoretical value ($\Sigma = -0.01$ C m^{-2}) and instead corresponded to a new value ($\Sigma = -0.1$ C m^{-2}). This confirmed our hypothesis that applying gate voltage increased the surface charge density by an order of magnitude. Upon closer inspection, there was a slight increase in the nanopore conductance from 10^{-3} to 10^{-5} M, followed by a small decrease at 10^{-6} M. This could be attributed to the fact that at very low concentrations, particularly below 10^{-3} M, subtle changes in the solution could impact the experimental results. Such appropriate fluctuations near the saturation point were generally acceptable. For a more detailed analysis, the experimental conductance (true label) and theoretical conductance (predicted label; $\Sigma = -0.01$, −0.05, and −0.1 C m^{-2}; concentration ranging from 10^{-6} to 1 M) were compared, and the confusion matrix were presented in Figure 3g–i. The color depth in the confusion matrix represented the proximity between predicted and experimental data points. For the predicted values of −0.01 and −0.05 C m^{-2}, the deviation from experimental values was evident, as shown by the deep color straying from the diagonal in Figure 3g, h. In contrast, when comparing the theoretical value of −0.1 C m^{-2}, the experimental values closely aligned with it, as indicated by the deep color closely following the diagonal and symmetrically distributed around it, as shown in Figure 3i. In summary, the application of gate voltage effectively enhances the surface charge density from −0.01 to −0.1 C m^{-2}.

2.4. Effect of Gate Voltage on Osmotic Energy Generation

Figure 4 further illustrates how the enhancement in surface charge density, induced directly by gate voltage (V_g), affected osmotic energy generation. The results showed that the I_{ion}-V_b response became more pronounced with increasing V_g (from 0 to −300 mV, step of −100 mV), as shown in Figure 4b. Both I_{sc} and V_{oc} increased synchronously, leading to a parallel rise in I_{os} (from 0.122 to 41.1 nA) and V_{os} (from 2.51 to 83.1 mV), as shown in Figure 4c. The V_{os} could be expressed as:[31]

$$V_{os} \approx \frac{k_B T}{ze} S \ln \frac{c_h}{c_l} \tag{2}$$

Here, $S = (D_+ - D_-)/(D_+ + D_-)$ represented the ionic selectivity, which was closely related to the surface charge density ($S = 1$ for ideal cation selectivity, $S = -1$ for ideal anion selectivity, and $S = 0$ for no selectivity). $D_\pm$ denoted the effective diffusion constant. k_b, T, and z represented the Boltzmann constant, temperature, and ion charge, respectively. At room temperature, $(k_B T)/(ze)$ was ≈25.7 mV.[31] With the introduction of the last terms ($c_h = 1$ M and $c_l = 1$ mM), S was calculated to increase from 0.0141 (indicating almost no selectivity) to 0.468 (indicating effective cation selectivity), as shown in Figure 4d. The corresponding energy conversion efficiency[31] ($\phi = S^2/2$) also increased to 10.9%. These results indicated that the increase in V_{os} was primarily due to the enhancement of ion selectivity, achieved through the gate-control reinforcement of surface charge density. This conclusion was further supported by simulation, as shown in Figure 4e. The simulation revealed a significant increase in cation concentration, coupled with a decrease in anion concentration, particularly near the pore surface, as the surface charge density increased from −0.01 to −0.03 C m^{-2}. This resulted in an amplification selectivity (S) between cations and anions. In addition, I_{os} could be further expressed as:[32]

$$I_{os} \approx \alpha \frac{2\pi r \Sigma}{L} \log \frac{c_h}{c_l} \tag{3}$$

Here, α represented a diffusion-osmotic mobility parameter, and r and L denoted the radius and length of the nanopore, respectively. Equation 3 accurately illustrates the proportional relationship between I_{os} and surface charge density (Σ). This indicated that the gate voltage exerted more direct and efficient control over I_{os}. The concurrent enhancement of V_{os} and I_{os} further facilitated a significant increase in osmotic power, as shown in Figure 4f. The single-pore power surged by four orders of magnitude from 0.315 pW to 2.90 nW, surpassing the previous

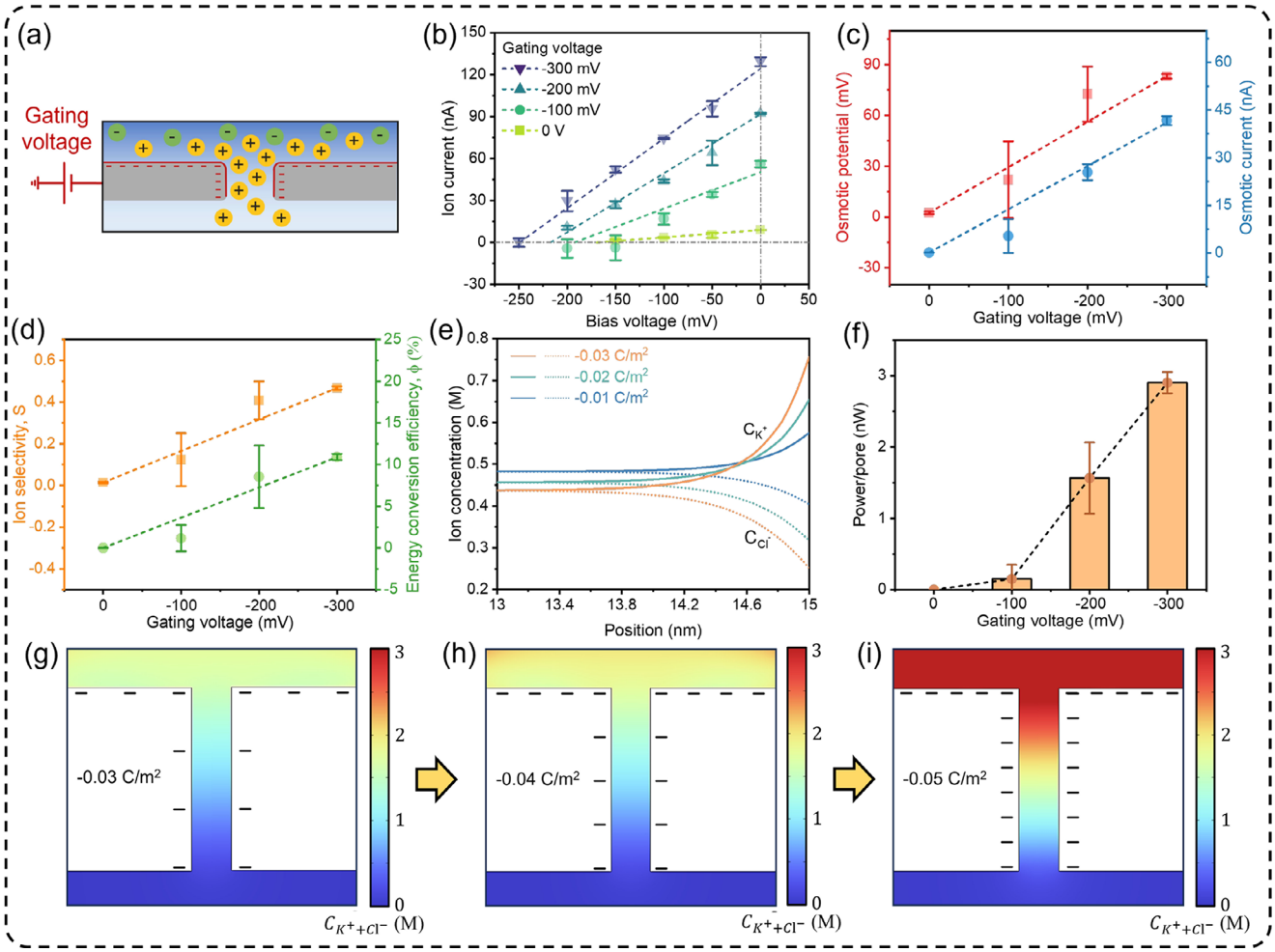

Figure 4. The effect of gate voltage (surface charge density) on osmotic energy generation. a) The diagram exhibited selective diffusion of positive ions resulting from the negative gate voltage imposed on the nanopore surface. b) With an increase in gate voltage, the I_{ion}-V_b response strengthened significantly. c) Meanwhile, the enlarged gate voltage also provoked a synchronous enhancement of I_{os} and V_{os}. d) These findings were attributed to the strengthening of ionic selectivity and ultimately contributed to higher energy conversion efficiency. e) The simulation results further argued that the C_{K+} near the nanopore surface was remarkably greater than the C_{Cl-}, and this tendency was even reinforced with an elevation of the surface charge density induced by the gate voltage. f) As a result, the generation power was boosted by 4 orders of magnitude from 0.315 pW (without gate voltage) to 2.90 nW (gate voltage of −300 mV). g–i) In-depth profiling of the simulation, the elevation of the surface charge density (gate voltage induced) was also beneficial in maintaining a higher concentration difference for osmotic energy generation. In summary, the increase in gate voltage resulted in the improvement of osmotic energy generation, due to the enhancement of surface charge density.

international record of 1 nW set by ultra-thin MoS_2.[16] Finally, the ion distribution simulations further demonstrated that a higher surface charge density contributed to maintaining a greater concentration difference across the membrane, as shown in Figure 4g–i. The initial boundary concentrations of K^+ and Cl^- were 2000 and 2 mM, respectively. However, with a lower surface charge density of −0.03 C m^{-2}, the actual concentration difference was reduced to 1428 mM, as shown in Figure 4g. This reduction was attributed to ionic diffusion and the ionic concentration polarization (ICP) effect,[33] which led to a diminished salinity difference (the real driving force) and decreased ion selectivity, adversely affecting the osmotic energy generation. Nevertheless, when the surface charge density was elevated to −0.05 C m^{-2}, the concentration difference immediately doubled to 2868 mM, as shown in Figure 4i. This enhancement ensured efficient outputs of I_{os} and V_{os}. In summary, the application of gate voltage not only directly improved surface charge density, thereby maintaining an effective salinity difference, but also indirectly enhanced ion selectivity, which collectively facilitated the osmotic energy generation in turn.

2.5. Ultrahigh-Performance Osmotic Energy Generation in Nanopore Arrays

Figure 5 further illustrates the capability of osmotic energy generation, extending from single pores to nanoporous membranes. The nanopore diameter was standardized at 30 nm, as it yielded the maximum power demonstrated in Figure S7 (Supporting Information). Additionally, an area of

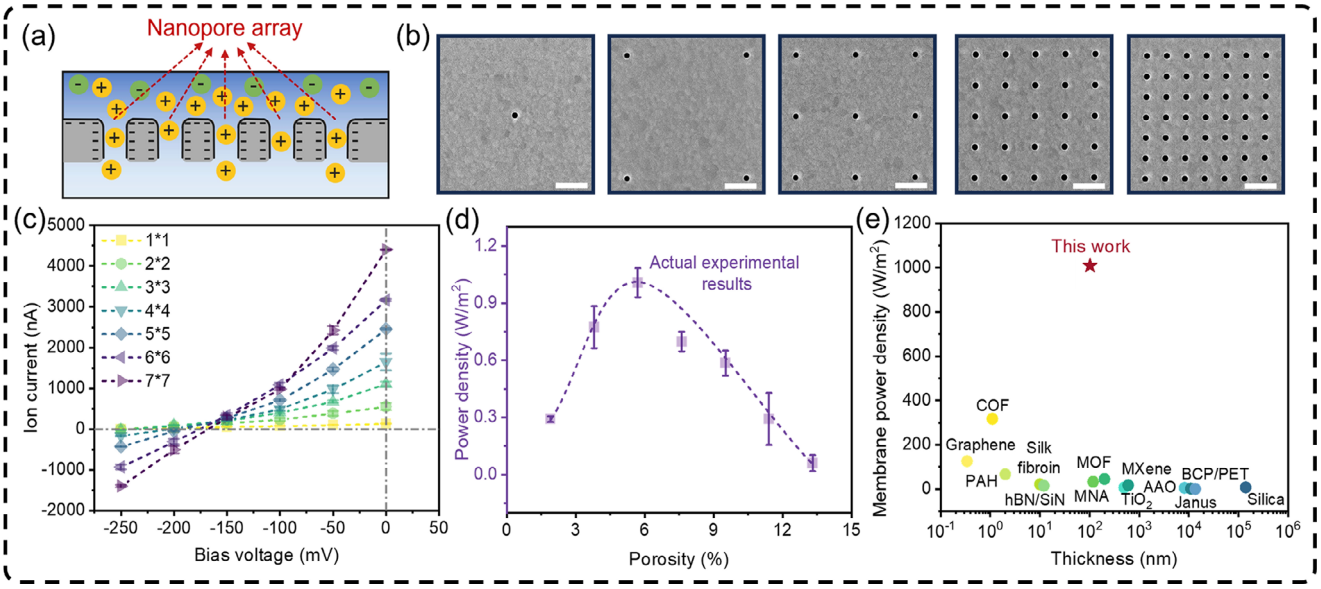

Figure 5. The ultrahigh-performance osmotic energy generation in nanopore arrays. a) A schematic representation of the nanopore arrays. b) Helium ion microscopy (HIM) images of nanopore arrays from 1 × 1 to 7 × 7 within the researching unit (1578 nm × 1578 nm). The scale bar was 400 nm. c) The I_{ion}-V_b response gradually enhanced with denser porosity. d) The summit of the ultrahigh-performance power density (1008 W m^{-2}) was achieved at the porosity of 5.7%. e) Compared with the state-of-the-art performances, our power density exceeded all the previous works. In summary, the power density of the porous membrane reached the pioneering of 1008 W m^{-2} on the global scale, via balancing the nanoporous density and the inter-pore effect.

1578 nm × 1578 nm (single-pore charging range required for −0.1 C m^{-2}) was chosen as the research unit to optimize the nanopore density while minimizing the inter-pore effect. The charged area directly related to surface charge density was regarded as the effective membrane area, as shown in Figure S6 (Supporting Information). Through simulations and linear fitting, the surface charged area required for ion selectivity saturation under different surface charge densities in nanopores was obtained. In other words, increasing the nanopore density within this range will lead to pore-pore interactions, making it meaningful to use this range as the research unit for nanopore arrays. By further balancing nanopore density and pore-pore interactions within this range, the maximum power density could be achieved. This method offers great extensibility and practicality. Each surface charge density can be associated with its corresponding effective membrane area. Furthermore, through additional simulations and calculations, the effective membrane area can also be determined for nanopores with different sizes, structures, and surface electrostatic properties. In this research, the nanopore array was progressively denser, ranging from 1 × 1 (porosity of 1.90%) to 7 × 7 (porosity of 13.3%), as shown in Figure 5b. As the number of nanopores increased, more transmembrane space was made available for ionic diffusion, resulting in a substantial increase in I_{sc} from 150 nA (1 × 1) to 4100 nA (7 × 7), as shown in the I_{ion}-V_b response in Figure 5c. This enhancement was also reflected in I_{os}, which increased from 25 to 250 nA, as shown in Figure S8b (Supporting Information). That was derived from the growth of the ion-passing area (radius, R) described by Equation 3. Notable, the output power density peaked at 1008 W m^{-2} with a porosity of 5.7%, as illustrated in Figure 5d. This issue is crucial for achieving large-scale application of nanopore-based osmotic energy generation. For this reason, most research articles on osmotic energy generation should address and discuss this topic in detail, and our paper is no exception. The second reason is that this issue has not yet been discussed in the context of gate-controlled nanopore systems, so we should fill this gap. The third reason is that we previously innovatively proposed using the charged area as the effective membrane area. Therefore, experimental validation is needed to confirm that this method can be truly implemented. This performance exceeded the state-of-the-art value of 317.5 W m^{-2} from covalent organic framework (COF) membranes by an order of magnitude,[34] as shown in Figure 5e and summarized in Table S3 (Supporting Information). The membrane power also reached a notable 10.0 nW (with a porosity of 5.7%), as compared to Figure S8c (Supporting Information). This ultrahigh performance could be attributed to two key factors. On one hand, the appropriate increase in nanopore density within the minimal research unit (single-pore required charging range) enhanced the ion flux across the membrane. On the other hand, the application of gate voltage enhanced surface charge density, maintaining the ion selectivity and concentration difference in each pore, thereby minimizing interference between adjacent pores as much as possible.

Nevertheless, further increasing the nanopore density led to a significant reduction in the pore gaps, causing an inadequate charging range to sustain the effective concentration difference across each pore in the array. This also resulted in a linear decline in ion selectivity, from 0.467 to 0.0310, as shown in Figure S8d (Supporting Information). Consequently, the performance deteriorated, with I_{os} decreasing from a peak of 250 to 150 nA, and V_{os} reducing linearly from 90 to 10 mV. This also resulted in a discrepancy between the actual power density and the

theoretical value predicted by single-pore linear extrapolation. Last but not least, inter-pore interactions in the array were investigated in depth from the perspective of the array gap and the array number, in Figures S10 and S11 (Supporting Information). In summary, higher power densities are expected to be achieved, by optimizing the nanopore density while maintaining ion selectivity and concentration differences across all pores with an adequate surface charge density.

3. Conclusion

In conclusion, reliable gate-controlled nanopores are developed as an efficient osmotic energy generator via the application of gate voltage and optimized array density. By leveraging multi-step MEMS and FIB etching with single-nanometer precision and direct visual feedback, a transistor-like multilayer of the gate-controlled nanopore can be precisely fabricated. Without additional complex modifications, the gate-controlled nanopores function as a nanofluid transistor, through the application of gate voltage alone, achieving bipolar response. Specifically, the gate voltage can enhance surface charge density to achieve high-selective ion diffusion, while maintaining an effective concentration difference across the nanopore. Power generation in a single pore has significantly increased by four orders of magnitude of 2.90 nW with gate involvement, surpassing the performance of pioneering 2D materials with sub-nanometer thickness. Additionally, the porous membrane has also reached a leading power density of 1008 nW m^{-2}, demonstrating the substantial potential for practical applications. Through comprehensive experiments and simulations, it has been found that balancing nanopore density while maintaining a defined charging region around each pore is crucial for the development of an optimal large-scale osmotic generator platform, from theoretical prediction to practical implementation.

This work not only advances the fundamental understanding of ionic transport in confined nanochannels but also paves new avenues for traditionally inefficient energy-conversion materials, such as silica, anodic aluminum oxide (AAO), polyethylene terephthalate (PET), and so on. Notably, with advancements in fabrication techniques, such as electron beam lithography, focused electron beam, and dielectric breakdown, biomimetic nanopores and nanochannels at sub-10 nm or even angstrom scales can be readily produced in inorganic materials, transforming them into ideal models for studying subcontinuum ion transport behavior.

4. Experimental Section

Characterization: An ellipsometry (TPY-1, wavelength 632.8 nm) was used to quantify the thickness of the suspending Si_3N_4 membrane. Utilizing a scanning electron microscope (Zeiss, Gemini 300), forward and backward imaging of the Si_3N_4 layer was accomplished. With a Ga^+ source in a focused ion beam (Zeiss, Orion NanoFab), the nanopore and corresponding cross-section were carved on the membrane. The ion beam current was 5 pA, while the accelerating voltage was 30 kV. During processing, real-time variations in nanopore diameter and morphology could be visualized with an He^+ source in a focused ion beam.

Electrochemical Measurement: Before testing, the nanopore film was thoroughly cleaned in Plasma (O_2 in 200 sccm, 200 W, 10 min) while improving the hydrophilicity of the nanopore surface. The nanopore film pasted in PCB was sandwiched between two Teflon cells to form fluid cells of *Cis* and *Trans*, respectively, buffered by two silicone gaskets in the middle. Ag/AgCl electrodes were placed on the *Cis* side as the source and *Trans* side as a drain to form a loop for accurate measurement of the ion current through the nanopore by source measure unit (Keithley, 2450). Each data point was recorded with ten significant figures, ensuring the full reliability of the data. In advance, the switchable gate voltage was applied directly to the Au layer of the nanopore through the wires in the PCB, utilizing another source measure unit. Unless otherwise specified, the default testing parameters were as follows: the ionic concentrations of *Cis*/*Trans* were 1 M/1 mM, the ionic type was KCl, and the nanopore diameter was 30 nm.

Simulation: The coupled Poisson–Nernst–Planck (PNP) and Navier–Stokes (NS) equations[27] were calculated in finite-element simulations to obtain accurate distributions of anions, cations, and potentials. Dense triangular grids (less than 0.1 nm) were applied to the nanopore surfaces that needed to be analyzed in detail, and the remaining positions were generated by the system. The ionic current was obtained using the following equation: $I = N_A \times e \int (J_{K^+} - J_{Cl^-})\, dS$. Here N_A is the Avogadro constant, e is the amount of charge per electron, J_{K^+} and J_{Cl^-} are the fluxes of potassium ions and chloride ions respectively, and S is the middle cross section of the nanopore, and the independent currents of I_{K^+} and I_{Cl^-} are obtained by integrating the respective fluxes separately. The ion selectivity based on the simulation was expressed by $S = (|I_+| - |I_-|)\,/(|I_+| + |I_-|)$. The ion concentrations on upper and lower nanopore surfaces were extracted from the center of the respective planes. The membrane potential was obtained by extracting the potential at the center of the nanopore.

Statistical Analysis: The experimental data were preprocessed to ensure accuracy and consistency. The data was presented in the form of mean ± standard deviation in the figures. For significant differences, the sample size was at least three, and one-way ANOVA was used to evaluate that between the groups while setting the confidence level ($p < 0.05$). Statistical analysis was performed using Origin software.

Supporting Information

Supporting Information is available from the Wiley Online Library or from the author.

Acknowledgements

This work was supported by the National Natural Science Foundation of China (22090050, 22176180, U24A20502), the National Key R&D Program of China (2021YFA1200403), the Natural Science Foundation of Hubei Province (2024AFA001), the Natural Science Foundation of Shenzhen (JCYJ20220530162406014).

Conflict of Interest

The authors declare no conflict of interest.

Author Contributions

X.L. and J.Z. contributed equally to this work. X.L. and Y.H. had the idea for the article. X.L., J.Z., and H.H. performed the search and data analysis. X.L. wrote the initial drafts of the work. Y.H., L.J., and Z.L. discussed the results and commented on the manuscript. All authors read and approved the final manuscript.

Data Availability Statement

The data that support the findings of this study are available in the supplementary material of this article.

Keywords

focused ion beam, gate-controlled nanopores, osmotic energy generation, solid-state nanopores

Received: January 11, 2025
Revised: March 1, 2025
Published online:

[1] Z. Liu, Z. Deng, G. He, H. Wang, X. Zhang, J. Lin, Y. Qi, X. Liang, *Nat. Rev. Earth Environ.* **2022**, *3*, 141.
[2] Y. Guo, M. Zhou, L. Peng, J. Yang, M. Li, J. Tian, L. Chen, D. L. Mauzerall, *Environ. Sci. Technol.* **2023**, *57*, 6494.
[3] M. R. Shaner, S. J. Davis, N. S. Lewis, K. Caldeira, *Energy Environ. Sci.* **2018**, *11*, 914.
[4] Y. Hu, H. Xiao, L. Fu, P. Liu, Y. Wu, W. Chen, Y. Qian, S. Zhou, X. Kong, Z. Zhang, L. Jiang, L. Wen, *Adv. Mater.* **2023**, *35*, 2301285.
[5] S. Li, J. Wang, Y. Lv, Z. Cui, L. Wang, *Adv. Funct. Mater.* **2024**, *34*, 2308176.
[6] B. E. Logan, M. Elimelech, *Nature* **2012**, *488*, 313.
[7] J. W. Post, H. V. M. Hamelers, C. J. N. Buisman, *Environ. Sci. Technol.* **2008**, *42*, 5785.
[8] J. N. Weinstein, F. B. Leitz, *Science* **1976**, *191*, 557.
[9] E. Guler, Y. Zhang, M. Saakes, K. Nijmeijer, *ChemSusChem* **2012**, *5*, 2262.
[10] X. Huang, Z. Zhang, X. Kong, Y. Sun, C. Zhu, P. Liu, J. Pang, L. Jiang, L. Wen, *Nano Energy* **2019**, *59*, 354.
[11] A. H. Avci, D. A. Messana, S. Santoro, R. A. Tufa, E. Curcio, G. Di Profio, E. Fontananova, *Membranes* **2020**, *10*, 168.
[12] R. A. Tufa, E. Curcio, W. van Baak, J. Veerman, S. Grasman, E. Fontananova, G. Di Profio, *RSC Adv.* **2014**, *4*, 42617.
[13] X. Lei, J. Zhang, H. Hong, Z. Yuan, Z. Liu, *Micromachines* **2022**, *13*, 923.
[14] Y. Fu, X. Guo, Y. Wang, X. Wang, J. Xue, *Nano Energy* **2019**, *57*, 783.
[15] K. Yazda, K. Bleau, Y. Zhang, X. Capaldi, T. Stdenis, P. Grutter, W. W. Reisner, *Nano Lett.* **2021**, *21*, 4152.
[16] J. Feng, M. Graf, K. Liu, D. Ovchinnikov, D. Dumcenco, M. Heiranian, V. Nandigana, N. R. Aluru, A. Kis, A. Radenovic, *Nature* **2016**, *536*, 197.
[17] X. Lei, J. Y. Zhang, H. Hong, J. T. Wei, Z. W. Liu, L. Jiang, *Small* **2023**, *19*, 2303370.
[18] S. W. Nam, M. J. Rooks, K. B. Kim, S. M. Rossnagel, *Nano Lett.* **2009**, *9*, 2044.
[19] N. Hu, Y. Ai, S. Qian, *Sens. Actuators, B* **2012**, *161*, 1150.
[20] M. Tsutsui, W. L. Hsu, D. Garoli, I. W. Leong, K. Yokota, H. Daiguji, T. Kawai, *ACS Nano* **2024**, *18*, 15046.
[21] E. B. Kalman, O. Sudre, I. Vlassiouk, Z. S. Siwy, *Anal. Bioanal. Chem.* **2009**, *394*, 413.
[22] R. B. M. Schasfoort, S. Schlautmann, J. Hendrikse, A. Van Den Berg, *Science* **1999**, *286*, 942.
[23] R. Ren, X. Wang, S. Cai, Y. Zhang, Y. Korchev, A. P. Ivanov, J. B. Edel, *Small Methods* **2020**, *4*, 2000356.
[24] L. Xue, H. Yamazaki, R. Ren, M. Wanunu, A. P. Ivanov, J. B. Edel, *Nat. Rev. Mater.* **2020**, *5*, 931.
[25] J. Wei, H. Hong, X. Wang, X. Lei, M. Ye, Z. Liu, *Nanoscale* **2024**, *16*, 18732.
[26] D. K. Kim, C. H. Duan, Y. F. Chen, A. Majumdar, *Microfluid. Nanofluid.* **2010**, *9*, 1215.
[27] I. Vlassiouk, S. Smirnov, Z. Siwy, *Nano Lett.* **2008**, *8*, 1978.
[28] C. Lee, L. Joly, A. Siria, A. L. Biance, R. Fulcrand, L. Bocquet, *Nano Lett.* **2012**, *12*, 4037.
[29] Y. Youn, S. Han, *Phys. Chem. Chem. Phys.* **2015**, *17*, 27806.
[30] R. B. Schoch, J. Y. Han, P. Renaud, *Rev. Mod. Phys.* **2008**, *80*, 839.
[31] M. Macha, S. Marion, V. V. R. Nandigana, A. Radenovic, *Nat. Rev. Mater.* **2019**, *4*, 588.
[32] A. Siria, P. Poncharal, A. L. Biance, R. Fulcrand, X. Blase, S. T. Purcell, L. Bocquet, *Nature* **2013**, *494*, 455.
[33] S. J. Kim, Y. C. Wang, J. H. Lee, H. Jang, J. Han, *Phys. Rev. Lett.* **2007**, *99*, 044501.
[34] J. L. Yang, B. Tu, G. J. Zhang, P. C. Liu, K. Hu, J. R. Wang, Z. Yan, Z. W. Huang, M. N. Fang, J. J. Hou, Q. J. Fang, X. H. Qiu, L. S. Li, Z. Y. Tang, *Nat. Nanotechnol.* **2022**, *17*, 622.